

Purcell-Induced Bright Single Photon Emitters in Hexagonal Boron Nitride

Mashnoon Alam Sakib,[#] Brandon Triplett,[#] William Harris, Naveed Hussain, Alexander Senichev, Melika Momenzadeh, Joshua Bocanegra, Polina Vabishchevich, Ruqian Wu, Alexandra Boltasseva, Vladimir M. Shalaev, and Maxim R. Shcherbakov*



Cite This: *Nano Lett.* 2024, 24, 12390–12397



Read Online

ACCESS |

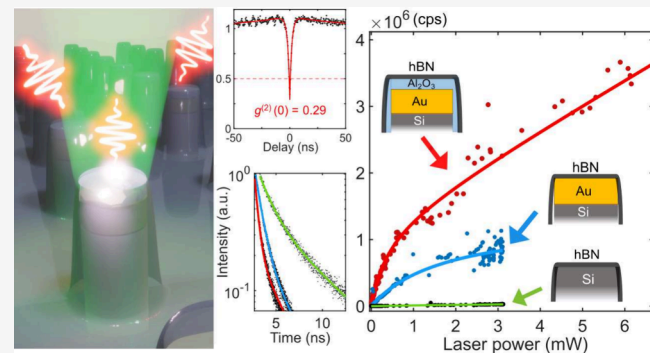
Metrics & More

Article Recommendations

Supporting Information

ABSTRACT: Single photon emitters (SPEs) in hexagonal boron nitride (hBN) are elementary building blocks for room-temperature on-chip quantum photonic technologies. However, fundamental challenges, such as slow radiative decay and non-deterministic placement of the emitters, limit their full potential. Here, we demonstrate large-area arrays of plasmonic nanoresonators (PNRs) for Purcell-induced room-temperature SPEs by engineering emitter-cavity coupling and enhancing radiative emission. Gold-coated silicon pillars with an alumina spacer enable a 10-fold local-field enhancement in the emission band of native hBN defects. We observe bright SPEs with an average saturated emission rate surpassing 5 million counts per second, an average lifetime of <0.5 ns, and 29% yield. Density functional theory reveals the beneficial role of an alumina spacer between hBN and gold, mitigating the electronic broadening of emission from defects proximal to the metal. Our results offer arrays of bright, heterogeneously integrated single-photon sources, paving the way for robust and scalable quantum information systems.

KEYWORDS: boron nitride, single photon emitters, plasmonic resonators, Purcell enhancement, density functional theory, quantum optics



Single photon emitters (SPEs) are essential in quantum photonic technologies, offering ways to revolutionize quantum computation, communication, and sensing systems.^{1–5} To enable the practical integration of SPEs into quantum photonic integrated circuits, these nonclassical light sources must possess a combination of properties that are challenging to achieve, including a high spontaneous emission rate,^{6–8} highly radiative quantum efficiency,⁹ room-temperature operation,¹⁰ and deterministic emitter placement.¹¹ Hexagonal boron nitride (hBN), a van der Waals material with a wide indirect bandgap of approximately 6 eV, is known to host room-temperature SPEs exhibiting zero-phonon line (ZPL) energies in the 1.5–2.2 eV range.^{10,12–18} The process of defect creation and activation usually requires techniques such as ion bombardment,¹⁹ irradiation and plasma engineering,^{20,21} thermal annealing,¹⁴ and UV-ozone treatment²² and results in the random spatial arrangement of defects. Achieving site-controlled activation and large-scale integration of SPEs into quantum photonic integrated circuits is, therefore, an active area of research. Previous works have attempted to deterministically place the emitters using focused ion beams,^{19,23} electron beams,^{11,24} femtosecond laser pulses,²⁵ and nanoindentation.²⁶ An alternative approach to inducing

defects by site damage is to activate and couple naturally occurring hBN defects with nanophotonic structures.^{27–31}

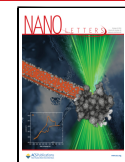
Efforts to improve hBN SPEs often entail designing nanoscale cavities that utilize quantum electrodynamic effects such as the Purcell effect, which alters their spontaneous emission rate.^{31–45} Previous works have used plasmonic nanostructures to create Purcell-enhanced emitter-cavity coupled systems.^{46–49} However, since plasmonic metals suffer from scattering and nonradiative losses, field-enhancing nanoantennas must meet stringent design and fabrication criteria for achieving an effective coupling to an emitter. Some of these requirements include spatial alignment of an emitter to the resonant cavity electric fields and an optimized gap between the emitter and nearby metallic surface to avoid quenching of fluorescence.^{34,50} An efficient plasmonic nanocavity-integrated antenna architecture using radiative decay

Received: June 11, 2024

Revised: September 11, 2024

Accepted: September 16, 2024

Published: September 23, 2024



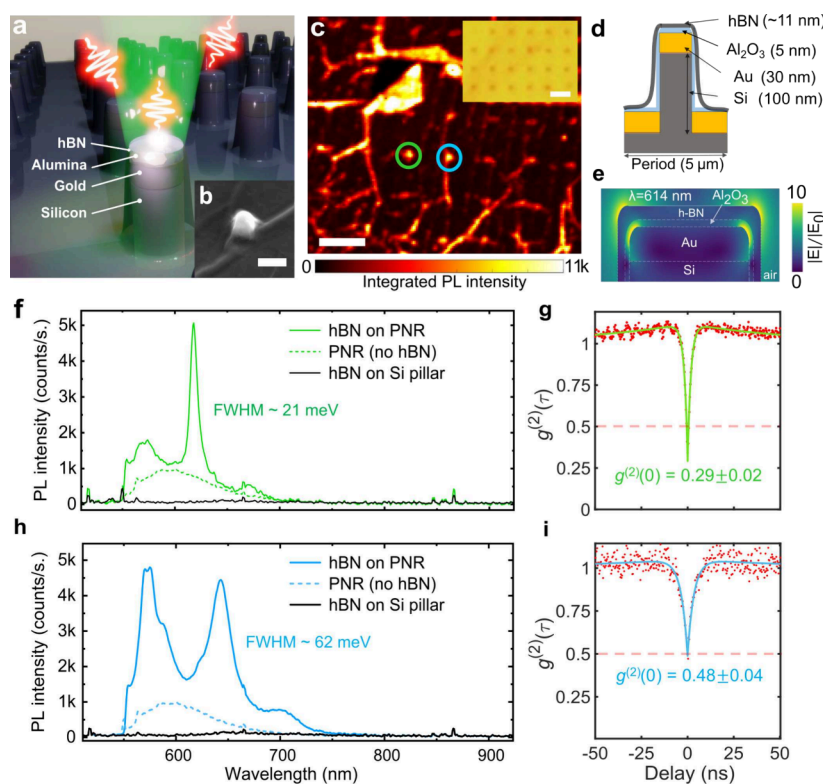


Figure 1. PNR-induced SPEs in hBN at room temperature. (a) Schematic of multilayer hBN coupled to a PNR. The hBN is separated from the plasmonic cavity by a 5 nm alumina spacer layer. The wave function in green and red indicates the Purcell-enhanced SPE absorbing and then emitting a photon. (b) Scanning electron microscopy image of a single PNR draped around with multilayer hBN. Scale bar is 500 nm. (c) A confocal scanning photoluminescence (PL) intensity map of a 6×7 emitter array containing hBN draped PNRs. Scale bar is 2 μm . Inset shows the optical image of the device; the scale bar is 5 μm . (d) Schematic cross-section of the hBN draped PNR. (e) Cross-sectional view of the simulated electric field enhancement $|E|/|E_0|$ distribution profile under normal illumination. The E-field distribution illustrates the confinement of the plasmonic hotspots at the resonator perimeter containing the draped hBN. (f) PL spectra for the device (hBN on PNR), background (PNR only), and hBN on Si pillar and (g) corresponding $g^{(2)}(\tau)$ from the emitter recorded from the green circled regions of the PL intensity mapping from (d). (h) PL spectra and (i) corresponding $g^{(2)}(\tau)$ from the emitter recorded from the blue circled regions of the PL intensity mapping from (d).

engineering approaches could have immense potential and far-reaching implications in both fundamental and applied research.

In this work, we achieve the on-site creation of optically activated, bright SPEs in a plasmonic nanoresonator (PNR) antenna architecture draped with unprocessed multilayer hBN. The gold-coated silicon nanopillars act as antenna nanoresonators supporting broadband surface plasmons that create hot spots with strong E-field confinement.⁵¹ The emitters, placed into near contact with the gold nanoparticles, experience a reduced spontaneous emission lifetime of less than 0.5 ns, while the typical nonresonant hBN defect emission lifetime lies in the 2–5 ns range.^{32–34,52–54} Additionally, we measured an average Purcell factor improvement of 2.46 with the incorporation of an alumina spacer. Radiative enhancement of photoluminescence (PL) resulted in bright room-temperature SPEs with sharp emission bandwidth down to sub-30 meV along with an average saturated photon count rate of more than 5 million counts/s. We also observed an SPE yield, determined by zero-delay second-order autocorrelation $g^{(2)}(0) < 0.5$, of approximately 29%. We performed density functional theory (DFT) calculations on SPEs hosted within hBN layers placed on gold. These calculations, supported by the experimental PL and $g^{(2)}(\tau)$ measurements, reveal electronic quenching for intrinsic defects in close proximity to gold. This work demonstrates a viable path toward realizing scalable,

room-temperature quantum photonic devices utilizing Purcell-enhanced bright SPEs in hBN.

PNR consists of a 30 nm-thick gold and a 5 nm-thick alumina spacer layer deposited on top of silicon pillar arrays with a height of 100 nm and a diameter of 160 nm. First, large-scale pillar arrays are fabricated in an intrinsic silicon substrate using electron beam lithography and reactive plasma etching. The pillars were coated with gold by e-beam evaporation and alumina by atomic layer deposition. A multilayer 11 nm-thick hBN film was wet-transferred onto the PNR array; see **Supplementary Section S1**. The hBN received no annealing, radiation, or other processes commonly used to create emitters. Upon the wet transfer, the hBN drapes around the PNR in a “tent-pole” profile (**Figure 1a**). **Figure 1b** shows a scanning electron microscope image of a representative PNR draped with hBN. **Figure 1c** represents a confocal scanning PL intensity map of the final assembled structure recorded at room temperature. Here, the spots with point-like emission marked with green and blue circles correspond to the regions where the transferred hBN is successfully draping the PNRs. The structural parameters with a cross-sectional geometry are illustrated schematically in **Figure 1d**. In **Figure 1e**, the fundamental plasmonic mode of hBN coupled to alumina-coated PNR is numerically calculated by the finite-difference time-domain (FDTD) method (**Supplementary Section S2**). The simulated electric field distribution shows that at 614 nm,

the gold nanoantenna stimulates E-fields in subwavelength volumes and gives rise to 10-fold enhanced plasmonic hot spots along the gold edges. This resonance wavelength is primarily determined by the size of the nanoantenna and its environment.^{7,55} When hBN is draped on PNRs, the emitters could potentially be placed in the vicinity of the PNR hot spots. When the emitters have a spectral and spatial overlap with the plasmonic modes, near-field enhancement takes place.^{32,52} According to the Purcell effect, in the weak-coupling regime, this helps in establishing an effective out-coupling between the emitter and the cavity and considerably increases the spontaneous emission rate of the systems.³² The alumina spacer layer can help in suppressing the emitter quenching.^{34,50}

Figure 1f represents PL recorded from the resonator site marked with the green circle in Figure 1c. The spectrum shows a sharp ZPL at 618 nm (2.01 eV) with a full width at half-maximum (fwhm) of 21 meV (Supplementary Section S3). This ZPL is accompanied by a 158 meV red-shifted phonon sideband (PSB) at 671 nm (1.85 eV). Second-order autocorrelation $g^{(2)}(\tau)$ measurements were performed at room temperature with a Hanbury-Brown and Twiss setup to record the nonclassical nature of SPEs from PNR-coupled hBN emitters. Figure 1g shows that the antibunching dip is at $g^{(2)}(0) = 0.29(\pm 0.02)$, proving that this hBN defect site is an SPE. Similarly, the PL spectra from the nearby emission site (blue circle in Figure 1d) are shown in Figure 1h. Two ZPL lines appear at 576 nm (ZPL₁ at 2.15 eV) and 643 nm (ZPL₂ at 1.93 eV), respectively. ZPL₂ had a PSB of 162 meV situated at 702 nm (1.76 eV). In both cases, the energy difference between ZPL and PSB lies within 160 ± 5 meV as reported previously¹⁴ (Supplementary Sections S4–S6). Various ZPL positions may be attributed to the variations in the local mechanical draping profile of the hBN along the different resonators. The antibunching measurement (Figure 1i) represents its SPE behavior with a $g^{(2)}(0) = 0.48(\pm 0.04)$. For the case of hBN on Si pillars, due to the absence of plasmonic resonance modes, the defect sites on Si pillars do not show quantum emission (Supplementary Section S2). We attribute this to the high refractive index and absorptivity of silicon that could potentially lead to emitter quenching.

Figure 2a shows the results of picosecond laser-assisted time-resolved PL measurements. We measured the emission lifetime across three samples with hBN draped over (1) silicon pillars (green), (2) PNRs with no alumina coating (blue), and (3) PNRs with a 5 nm-thick alumina spacer coating (red), respectively. The highlighted recorded lifetimes for hBN on PNRs with alumina coating (red) and without any alumina coating (blue), are 998 and 473 ps, respectively. The recorded emission lifetime for hBN on silicon pillars reaches 2.3 ns. We measured the fluorescence lifetime across 23 different emitters both in the presence and in the absence of an alumina layer (Figure 2b). Without alumina, the average recorded average lifetime is 1180 ps. For alumina-coated PNRs, the average lifetime is 480 ps, showing a 2.46-fold reduction. Note that the typical defect lifetimes reported earlier for hBN land in the range of 2–5 ns,^{10,11,14,21,26,27,31} which is ≈ 4 –10 times longer than our observations for the PNR-coupled hBN, denoting significant Purcell enhancement of spontaneous emission (F_p).^{7,32} We express F_p as the ratio of the emitter transition rate (Γ) with the hBN on PNRs to each the native emitter transition rate and the nonalumina emitter transition rate (Γ_0). Here, the transition rate is the sum of the radiative and nonradiative transition rates. F_p can be defined as the inverse

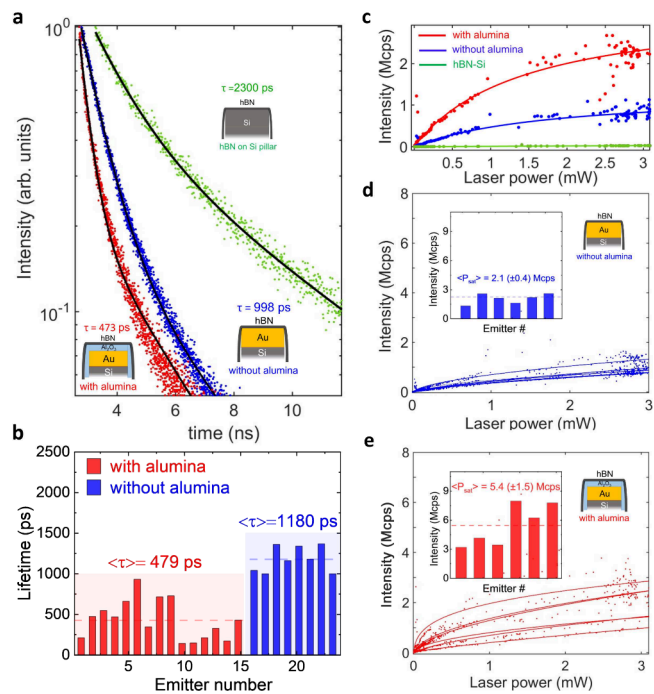


Figure 2. Purcell-enhanced photophysical characteristics of SPEs in hBN. (a) Time-resolved PL decay showing radiative transition lifetimes recorded from three different device configurations with hBN draped on alumina coated PNR (red dot), PNR without alumina (blue dot), and silicon pillar (green dot). Solid lines represent corresponding fits to a biexponential decay function model. (b) Histogram showing the statistical distribution of radiative transition lifetimes recorded from time-resolved photoluminescence measurements of 23 photon emitters recorded from hBN on alumina-coated PNR (red box) and PNR without alumina (blue box) (c) Fluorescence saturation measurements recorded from three different device configurations mentioned in (a). (d)-(e) saturation measurements recorded from a total of 12 photon emitters across devices with hBN on PNRs (d) without alumina and (e) with alumina. Insets in (d) - (e) show corresponding histogram of saturated photon count rates. Corresponding fits in solid lines are plotted using a first-order saturation model.

ratio of the lifetime of the emitter (τ) with hBN on PNRs to each the native emitter lifetime and the nonalumina emitter lifetime (τ_0):

$$F_p = \frac{\Gamma}{\Gamma_0} = \frac{\Gamma_r + \Gamma_{nr}}{\Gamma_0} = \frac{\tau_0}{\tau} \quad (1)$$

where Γ_r and Γ_{nr} are radiative and nonradiative rates, respectively. This reduction in lifetime suggests a spontaneous emission Purcell-enhancement by a factor of 2.46 when comparing only the improvement by the alumina and up to ~ 10 when comparing to the nonplasmonic pillar cases in the literature.^{27,31}

The presence of an alumina spacer layer allows for higher Purcell enhancement by suppressing emitter quenching. Figure 2 (c) - (e) characterize fluorescence saturation photon count rates across the three cases by measuring the PL intensity as a function of the excitation power. To extract the saturated single-photon count rates, we corrected the measured data sets for the background emission and fitted them using the first-order saturation model:

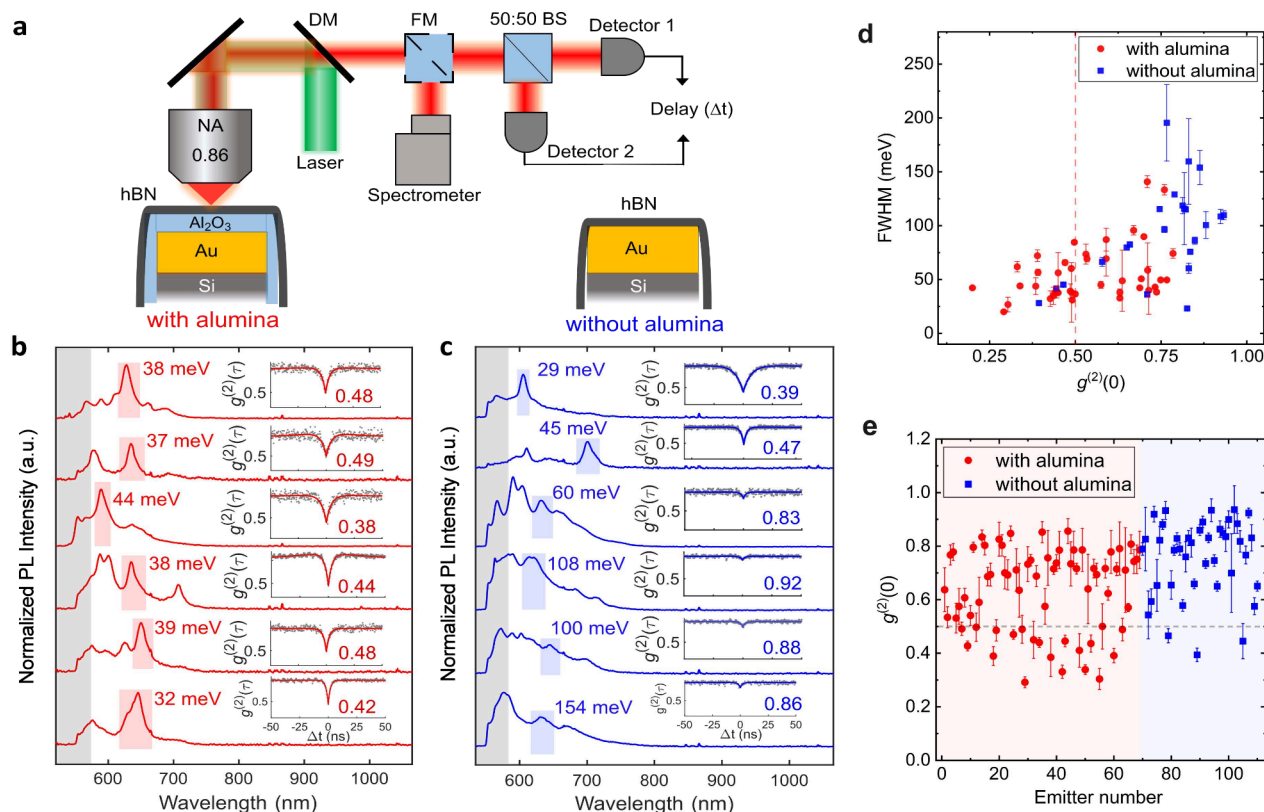


Figure 3. Optical characterization of Purcell-induced SPEs. (a) Simplified schematic of the confocal PL setup integrated with a Hanbury-Brown and Twiss (HBT) interferometer that was used to record PL intensity and second-order autocorrelation $g^{(2)}(\tau)$ measurements at room temperature. The objective lens, reflecting mirror, dichroic mirror, flippable mirror, beam splitter, and single avalanche photon detectors are denoted by Obj., DM, FM, BS, and Detector, respectively. (b and c) Normalized PL spectra of six representative photon emitters and (insets) corresponding $g^{(2)}(\tau)$ measurements recorded from hBN on PNR (b) with alumina and (c) without alumina. The spectra are normalized without background correction and offset vertically. The solid traces in the insets represent theoretical fits to the recorded $g^{(2)}(\tau)$ data. (d) The fwhm and the antibunching dip $g^{(2)}(0)$ values extracted from measurements recorded for 65 PNR-coupled emitters. (e) Scatter plot of the $g^{(2)}(0)$ values extracted from a total of 110 emitters from hBN on PNR with alumina (red dot) and without alumina (blue dot) device configurations. The error bars represent their corresponding fitting uncertainties. Background subtraction has not been applied to any recorded autocorrelation data.

$$I(P) = \frac{I_{\infty} P}{P_{\text{sat}} + P} \quad (2)$$

where I_{∞} and P_{sat} are fitting parameters corresponding to the saturated emission rate and saturation power, respectively.^{11,14,56,57} In the case of hBN on PNRs with alumina (red) and without alumina (blue), the saturated emission rates were 3.4 million counts/s (Mcps) ($P_{\text{sat}} = 1.4$ mW) and 1.3 Mcps ($P_{\text{sat}} = 1.8$ mW), respectively. For hBN on Si pillars (green), I_{∞} was 0.18 Mcps ($I_{\infty} = 1.7$ mW) (Supplementary Section S8). The overall PL enhancement factor for hBN on PNR with alumina is 2.28 (Supplementary Section S9), compared to the hBN on PNR without alumina suggesting the radiative enhancement for saturation intensities are comparable to the maximum Purcell enhancements achieved through radiative lifetime measurements (Figures 2a,b and Supplementary Section S9). Overall, in the case of hBN coupled to alumina-coated PNRs, the efficiently localized E-field and suppressed nonradiative leakage allow the Purcell-enhanced cavity dynamics to accelerate the spontaneous emission decay rate toward realizing fast and bright SPEs.

To gain insights into the Purcell-enhanced SPEs, we recorded PL and corresponding $g^{(2)}(\tau)$ measurements at room temperature from 65 emitters. The experimental setup is described in Supplementary Section S11. We measured two

device configurations, one in which the hBN film is coupled to PNRs with alumina and one without, as shown in Figure 3a. Figures 3b,c show examples of PL spectra and corresponding $g^{(2)}(\tau)$ measurements for the two cases, respectively. In Figure 3b, PL spectra show that emission mostly occurs between 585 nm (2.11 eV) and 675 nm (1.83 eV). These spectra also show that emitters coupled to the alumina, on average, had narrower emission fwhm as compared to the latter case of PNRs without alumina. The alumina coating acts as a dielectric spacer preventing electromagnetic quenching and homogenizing the local density of photonic states. This effect has been theoretically predicted for deep-subwavelength nanoresonators.^{32,33,52} When the hBN was in direct contact with the gold without the spacer, the recorded PL spectra (Figure 3c) mostly consisted of multiple spectral peaks that had lower relative intensities as compared to the case with the spacer. In Figure 3d, the emission fwhm and corresponding $g^{(2)}(0)$ are plotted for 65 representative emitters recorded from hBN draped on PNRs with alumina (red dots) and without alumina (blue squares). In the presence of alumina, the emitters achieved an overall average sub-50 meV emission, with 20 out of the 69 emitters behaving as SPEs with $g^{(2)}(0) < 0.5$, providing a yield of approximately 29%. For the case without alumina, the emission becomes broader with an average fwhm of over 90 meV, and 3 out of 41 emitters are SPEs, which is less than

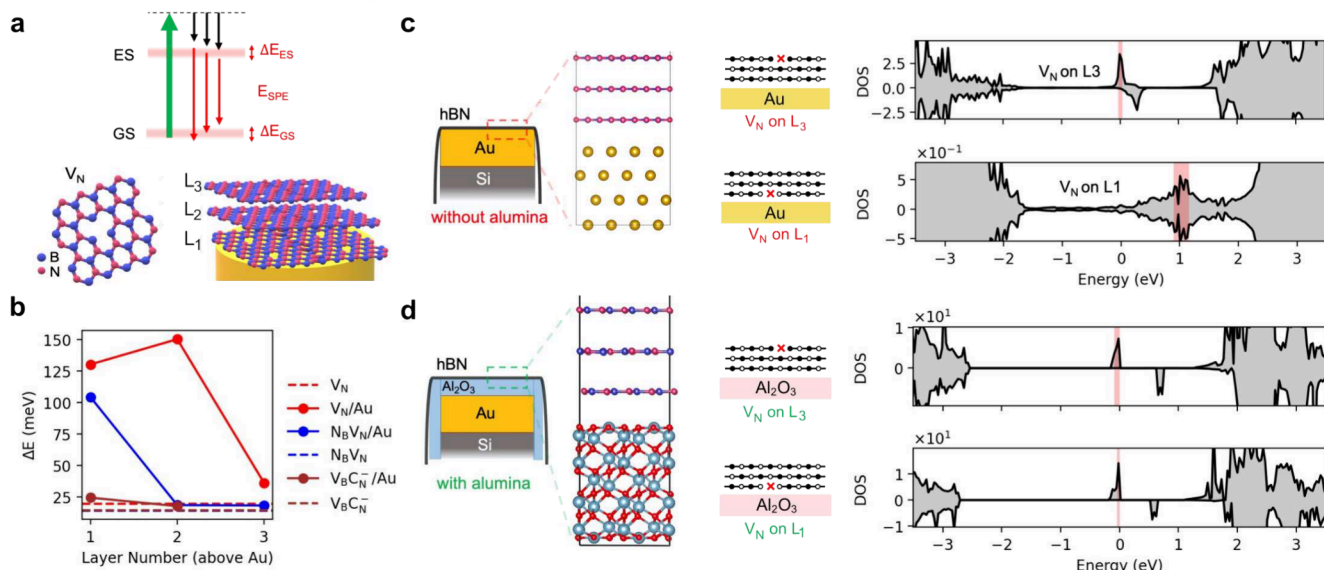


Figure 4. (a) Energy diagram depicting the effect of electronic broadening of the midgap states on single photon emission (top). Schematic illustration of defect structure V_N (bottom left) within hBN as analyzed through DFT calculations. V_N is considered at three positions (L_1 , L_2 , and L_3) above a gold (Au) slab. (bottom right). (b) fwhm of the V_N (red), $N_B V_N$ (blue), and $V_B C_N^-$ (brown) DFT midgap states as a function of layer number from the Au surface. Dashed lines correspond to defect structures in the absence of Au. The L_3 position of $V_B C_N^-$ is not considered due to significant out-of-plane deformation in defects on the top layer, which is not relevant to the study of proximity effects. (c) Illustration of the hBN on PNR without alumina and the corresponding structures used in DFT calculations. Partial density of states (DOS) integrated over the three-layer hBN/Au system in two configurations: with V_N on the top layer (L_3) and V_N on the bottom layer closest to Au (L_1). fwhm of the midgap states shaded in red shows significant broadening from the interaction with Au. (d) Similar DOS calculations as in (c) but evaluated for the case of hBN on PNRs with the alumina spacer layer.

10%. This observation suggests that the presence of the alumina spacer helps in boosting the success rate of SPE formation.

We note that emitters from samples without an alumina spacer exhibit broader average line widths (Figure 3d) and a degraded $g^{(2)}(0)$ (Figure 3e). One reason could be the coupling to the image charge in gold, which may lead to damped single-photon transitions. However, the time-bandwidth product of the single photon peaks significantly exceeds unity, indicating that peak widths are not primarily determined by transition lifetimes. Thus, image-charge-induced damping does not fully explain the variation in the line widths. To better understand the line widths and SPE purity, we used DFT with a model of a hBN/gold interface. We perform DFT calculations for a model system of three-layer hBN supported on gold, with results separately obtained for defects on each layer to characterize proximity effects.

Our emitter creation technique does not involve any active preprocessing. The hBN is draped over PNRs without any specific defect activation process and thus emission is most likely to originate from native hBN defects. We recorded confocal PL measurements from 73 hBN-draped PNR sites that statistically suggest the emitter ZPLs are mostly in the 1.92–2.17 eV range (Supplementary Figure S14a) with an average separation energy between ZPL and PSB of 165 ± 10 meV (Supplementary Figure S14b). We find this experimentally acquired ZPL and PSB emission band statistics to be most consistent with hBN's intrinsic defects, such as a nitrogen vacancy (V_N) and an antisite complex in which the nitrogen occupies the boron site, and there is a missing atom at the nitrogen site ($N_B V_N$).^{10,58–60} It has been demonstrated, however, that the hBN SPEs at ~ 2 eV likely come from carbon⁶¹ and organic molecules-related⁶² defects. These defect

candidates can result in significant out-of-plane deformation with sensitivity to the local environment. This environment sensitivity may help to explain the range of variations in the ZPL peak positions that are observed experimentally.

We perform DFT calculations on the less environment-sensitive charge-neutral defects V_N and $N_B V_N$ to illustrate the proximity broadening effect in the absence of large structural deformations. Moreover, we also analyze the carbon-based defect $V_B C_N^-$ as it is believed to host a transition consistent with experimental observations of SPE.⁶¹ Moreover, it has been reported that SiO_2 nanostructures^{27,30} and mechanically strained polymer slabs²⁹ can induce strain that modifies the electronic band structure of hBN defects and enables single photon emission. Throughout our experiment, SPE behavior is only found in the case of hBN on PNRs (Figures 1f–1i). It should, however, be noted that for the case of hBN on Si pillars, no SPE emission is found. As a result, we attribute that in the case of hBN with PNRs, there could be a synergistic effect arising from a combination of a minimal strain-perturbation and a plasmonic mode coupling mechanism likely playing an important role in achieving PNRs' Purcell-induced SPE phenomenon.

DFT calculations reveal that defects in proximity to gold may broaden the midgap states, facilitating numerous nearly degenerate single-photon transitions and thus broader line widths (see conceptual diagram in Figure 4a). The fwhm of midgap states for V_N , $N_B V_N$ and $V_B C_N^-$ are found to be significantly larger for defects positioned near Au (Figure 4b). For instance, the electronic density of states (DOS) for a V_N defected hBN/Au structure shows a narrow midgap peak when the defect is positioned on layer 3 above Au, and a much broader peak when the defect is on the closest layer, layer 1, above Au (Figure 4c). Additionally, charge transfer from the

Au to the hBN is evident, manifesting as demagnetization and the “filling in” of the band gap. While the influence of gold is found to rapidly diminish with layer depth, the electric field enhancement strongly localizes near the hBN/Au interface (Supplementary Figure S18e), where electronic effects are likely still relevant. In contrast, an alumina spacer leads to a more evenly distributed field across hBN (Supplementary Figure S18e), suggesting that the observed defect states are less likely to be positioned near an interface. We further observe negligible broadening when hBN is supported on alumina (Figure 4d), in contrast to the significant broadening seen in the case of gold. These findings help explain the differences in the emission characteristics of SPEs with and without an alumina spacer and support the beneficial role of an insulating layer between hBN and Au.

In summary, we have demonstrated a PNR antenna architecture for the experimental realization of Purcell-enhanced SPEs in hBN at room temperature. We have shown activation and enhancement of hBN SPEs by utilizing the coupling of natural hBN defects with the resonance modes of the PNR platform, accelerating the coupled emitters’ spontaneous emission rate. An average of 2.46-fold reduction in SPE lifetime, down to an average of 480 ps, is observed for bright SPEs with an average saturated photon count rate of more than 5 million counts/s and a yield of 29%. We also find that suppression of line broadening by the use of an alumina spacer layer is favorable to the performance and yield of the emitters. DFT calculations further emphasize the beneficial role of the alumina spacer for intrinsic defects in hBN by SPE line width broadening mitigation. Our findings highlight the potential of natural defects in unprocessed hBN on resonant nanostructures as a versatile platform for Purcell-enhanced bright SPEs, offering stable operation at room temperature and emission across a broad spectral range. Our results represent an important step toward scalable room-temperature light-based quantum information systems.

■ ASSOCIATED CONTENT

SI Supporting Information

The Supporting Information is available free of charge at <https://pubs.acs.org/doi/10.1021/acs.nanolett.4c02581>.

Details of sample fabrication, wet-transfer, Raman-, and AFM-characterization of hBN, details of FDTD simulations, experimental setup, and structural and optical characterization of various PNR devices draped with hBN; details of spectral analysis of SPE PL and $g^{(2)}(\tau)$ measurements; laser power-dependent $g^{(2)}(\tau)$ and fluorescence saturation; details of DFT calculation for native hBN defect models on gold; and references (PDF)

■ AUTHOR INFORMATION

Corresponding Author

Maxim R. Shcherbakov – Department of Electrical Engineering and Computer Science and Department of Materials Science and Engineering, University of California, Irvine, California 92697, United States;  orcid.org/0000-0001-7198-5482; Email: maxim.shcherbakov@uci.edu

Authors

Mashnoon Alam Sakib – Department of Electrical Engineering and Computer Science, University of California, Irvine, California 92697, United States

Brandon Triplett – Elmore Family School of Electrical and Computer Engineering, Birck Nanotechnology Center and Purdue Quantum Science and Engineering Institute, Purdue University, West Lafayette, Indiana 47907, United States; Quantum Science Center (QSC), a National Quantum Information Science Research Center of the U.S. Department of Energy (DOE), Oak Ridge National Laboratory, Oak Ridge, Tennessee 37931, United States

William Harris – Department of Physics and Astronomy, University of California, Irvine, California 92697, United States

Naveed Hussain – Department of Electrical Engineering and Computer Science, University of California, Irvine, California 92697, United States

Alexander Senichev – Elmore Family School of Electrical and Computer Engineering, Birck Nanotechnology Center and Purdue Quantum Science and Engineering Institute, Purdue University, West Lafayette, Indiana 47907, United States; Quantum Science Center (QSC), a National Quantum Information Science Research Center of the U.S. Department of Energy (DOE), Oak Ridge National Laboratory, Oak Ridge, Tennessee 37931, United States;  orcid.org/0000-0003-2789-123X

Melika Momenzadeh – Department of Electrical Engineering and Computer Science, University of California, Irvine, California 92697, United States

Joshua Bocanegra – Department of Physics and Astronomy, University of California, Irvine, California 92697, United States

Polina Vabishchevich – Department of Chemistry and Biochemistry, University of Maryland, College Park, Maryland 20742, United States;  orcid.org/0000-0003-0795-2314

Ruqian Wu – Department of Physics and Astronomy, University of California, Irvine, California 92697, United States;  orcid.org/0000-0002-6156-7874

Alexandra Boltasseva – Elmore Family School of Electrical and Computer Engineering, Birck Nanotechnology Center and Purdue Quantum Science and Engineering Institute, Purdue University, West Lafayette, Indiana 47907, United States; Quantum Science Center (QSC), a National Quantum Information Science Research Center of the U.S. Department of Energy (DOE), Oak Ridge National Laboratory, Oak Ridge, Tennessee 37931, United States;  orcid.org/0000-0001-8905-2605

Vladimir M. Shalaev – Elmore Family School of Electrical and Computer Engineering, Birck Nanotechnology Center and Purdue Quantum Science and Engineering Institute, Purdue University, West Lafayette, Indiana 47907, United States; Quantum Science Center (QSC), a National Quantum Information Science Research Center of the U.S. Department of Energy (DOE), Oak Ridge National Laboratory, Oak Ridge, Tennessee 37931, United States

Complete contact information is available at:

<https://pubs.acs.org/doi/10.1021/acs.nanolett.4c02581>

Author Contributions

[#](M.A.S. and B.T.) Contributed equally to this work.

Notes

The authors declare no competing financial interest.

ACKNOWLEDGMENTS

The authors acknowledge stimulating discussions with Igor Aharonovich, Sejeong Kim, and Vahagn Mkhitaryan. This work is supported by the National Science Foundation (ECCS-2339271), Defense Advanced Research Projects Agency (D22AP00153), U.S. Department of Energy (DOE), Office of Science through the Quantum Science Center (QSC), DE-AC05-00OR22725 and the Air Force Office of Scientific Research (AFOSR) grant FA9550-22-1-0372. M.A.S. acknowledges support from Eddleman Quantum Institute at the University of California, Irvine. P.V. acknowledges support under the Professional Research Experience Program (PREP), funded by the National Institute of Standards and Technology and administered through the Department of Chemistry and Biochemistry, University of Maryland.

REFERENCES

(1) Aharonovich, I.; Englund, D.; Toth, M. Solid-state single-photon emitters. *Nat. Photonics* **2016**, *10*, 631–641.

(2) Atatüre, M.; Englund, D.; Vamivakas, N.; Lee, S. Y.; Wrachtrup, J. Material platforms for spin-based photonic quantum technologies. *Nat. Rev. Mater.* **2018**, *3*, 38.

(3) Degen, C. L.; Reinhard, F.; Cappellaro, P. Quantum sensing. *Rev. Mod. Phys.* **2017**, *89*, 035002.

(4) Weber, J. R.; Koehl, W. F.; Varley, J. B.; Janotti, A.; Buckley, B. B.; Van De Walle, C. G.; Awschalom, D. D. Quantum computing with defects. *Proc. Natl. Acad. Sci. U. S. A.* **2010**, *107*, 8513.

(5) O'Brien, J. L.; Furusawa, A.; Vučković, J. Photonic quantum technologies. *Nat. Photonics* **2009**, *3*, 687–695.

(6) Russell, K. J.; Liu, T.-L.; Cui, S.; Hu, E. L. Large spontaneous emission enhancement in plasmonic nanocavities. *Nat. Photonics* **2012**, *6*, 459–462.

(7) Akselrod, G. M.; Argyropoulos, C.; Hoang, T. B.; Ciraci, C.; Fang, C.; Huang, J.; Smith, D. R.; Mikkelsen, M. H. Probing the mechanisms of large Purcell enhancement in plasmonic nanoantennas. *Nat. Photonics* **2014**, *8*, 835–840.

(8) Schietinger, S.; Barth, M.; Aichele, T.; Benson, O. Plasmon-enhanced single photon emission from a nanoassembled metal-diamond hybrid structure at room temperature. *Nano Lett.* **2009**, *9*, 1694–1698.

(9) Claudon, J.; Bleuse, J.; Malik, N. S.; Bazin, M.; Jaffrennou, P.; Gregersen, N.; Sauvan, C.; Lalanne, P.; Gérard, J.-M. A highly efficient single-photon source based on a quantum dot in a photonic nanowire. *Nat. Photonics* **2010**, *4*, 174–177.

(10) Tran, T. T.; Bray, K.; Ford, M. J.; Toth, M.; Aharonovich, I. Quantum emission from hexagonal boron nitride monolayers. *Nat. Nanotechnol.* **2016**, *11*, 37–41.

(11) Fournier, C.; Plaud, A.; Roux, S.; Pierret, A.; Rosticher, M.; Watanabe, K.; Taniguchi, T.; Buil, S.; Quelin, X.; Barjon, J.; et al. Position-controlled quantum emitters with reproducible emission wavelength in hexagonal boron nitride. *Nat. Commun.* **2021**, *12*, 3779.

(12) Cassabois, G.; Valvin, P.; Gil, B. Hexagonal boron nitride is an indirect bandgap semiconductor. *Nat. Photonics* **2016**, *10*, 262–266.

(13) Chejanovsky, N.; Rezai, M.; Paolucci, F.; Kim, Y.; Rendler, T.; Rouabeh, W.; Fávaro de Oliveira, F.; Herlinger, P.; Denisenko, A.; Yang, S.; Gerhardt, I.; Finkler, A.; Smet, J.; Wrachtrup, J. Structural attributes and photodynamics of visible spectrum quantum emitters in hexagonal boron nitride. *Nano Lett.* **2016**, *16*, 7037–7045.

(14) Tran, T. T.; Elbadawi, C.; Totonjian, D.; Lobo, C. J.; Grosso, G.; Moon, H.; Englund, D. R.; Ford, M. J.; Aharonovich, I.; Toth, M. Robust multicolor single photon emission from point defects in hexagonal boron nitride. *ACS Nano* **2016**, *10*, 7331–7338.

(15) Grosso, G.; Moon, H.; Lienhard, B.; Ali, S.; Efetov, D. K.; Furchi, M. M.; Jarillo-Herrero, P.; Ford, M. J.; Aharonovich, I.; Englund, D. Tunable and high-purity room temperature single-photon emission from atomic defects in hexagonal boron nitride. *Nat. Commun.* **2017**, *8*, 705.

(16) Pelliciari, J.; Mejia, E.; Woods, J. M.; Gu, Y.; Li, J.; Chand, S. B.; Fan, S.; Watanabe, K.; Taniguchi, T.; Bisogni, V.; Grosso, G. Elementary excitations of single-photon emitters in hexagonal Boron Nitride. *Nat. Mater.* **2024**, *23*, 1230.

(17) Azzam, S. I.; Parto, K.; Moody, G. Prospects and challenges of quantum emitters in 2D materials. *Appl. Phys. Lett.* **2021**, *118*, 240502.

(18) Turiansky, M. E.; Parto, K.; Moody, G.; Van de Walle, C. G. Rational design of efficient defect-based quantum emitters. *APL Photonics* **2024**, *9*, 066117.

(19) Glushkov, E.; Macha, M.; Rath, E.; Navikas, V.; Ronceray, N.; Cheon, C. Y.; Ahmed, A.; Avsar, A.; Watanabe, K.; Taniguchi, T.; Shorubalko, I.; Kis, A.; Fantner, G.; Radenovic, A. Engineering optically active defects in hexagonal boron nitride using focused ion beam and water. *ACS Nano* **2022**, *16*, 3695–3703.

(20) Fischer, M.; Caridad, J. M.; Sajid, A.; Ghaderzadeh, S.; Ghorbani-Asl, M.; Gammelgaard, L.; Bøggild, P.; Thygesen, K. S.; Krasheninnikov, A. V.; Xiao, S.; Wubs, M.; Stenger, N. Controlled generation of luminescent centers in hexagonal boron nitride by irradiation engineering. *Sci. Adv.* **2021**, *7*, eabe7138.

(21) Xu, Z.-Q.; et al. Single photon emission from plasma treated 2D hexagonal boron nitride. *Nanoscale* **2018**, *10*, 7957–7965.

(22) Li, C.; Xu, Z.-Q.; Mendelson, N.; Kianinia, M.; Toth, M.; Aharonovich, I. Purification of single-photon emission from hBN using post-processing treatments. *Nanophotonics* **2019**, *8*, 2049–2055.

(23) Klaiss, R.; Ziegler, J.; Miller, D.; Zappitelli, K.; Watanabe, K.; Taniguchi, T.; Alemán, B. Uncovering the morphological effects of high-energy Ga+ focused ion beam milling on hBN single-photon emitter fabrication. *J. Chem. Phys.* **2022**, *157*, 074703.

(24) Kumar, A.; Cholsuk, C.; Zand, A.; Mishuk, M. N.; Matthes, T.; Eilenberger, F.; Suwanna, S.; Vogl, T. Localized creation of yellow single photon emitting carbon complexes in hexagonal boron nitride. *APL Mater.* **2023**, *11*, 071108.

(25) Gan, L.; Zhang, D.; Zhang, R.; Zhang, Q.; Sun, H.; Li, Y.; Ning, C.-Z. Large-scale, high-yield laser fabrication of bright and pure single-photon emitters at room temperature in hexagonal boron nitride. *ACS Nano* **2022**, *16*, 14254–14261.

(26) Xu, X.; Martin, Z. O.; Sychev, D.; Lagutchev, A. S.; Chen, Y. P.; Taniguchi, T.; Watanabe, K.; Shalaev, V. M.; Boltasseva, A. Creating quantum emitters in hexagonal boron nitride deterministically on chip-compatible substrates. *Nano Lett.* **2021**, *21*, 8182–8189.

(27) Proscia, N. V.; Shotan, Z.; Jayakumar, H.; Reddy, P.; Cohen, C.; Dollar, M.; Alkauskas, A.; Doherty, M.; Meriles, C. A.; Menon, V. M. Near-deterministic activation of room-temperature quantum emitters in hexagonal boron nitride. *Optica* **2018**, *5*, 1128–1134.

(28) Ziegler, J.; Klaiss, R.; Blaikie, A.; Miller, D.; Horowitz, V. R.; Alemán, B. J. Deterministic quantum emitter formation in hexagonal boron nitride via controlled edge creation. *Nano Lett.* **2019**, *19*, 2121–2127.

(29) Mendelson, N.; Doherty, M.; Toth, M.; Aharonovich, I.; Tran, T. T. Strain-induced modification of the optical characteristics of quantum emitters in hexagonal boron nitride. *Adv. Mater.* **2020**, *32*, 1908316.

(30) Chen, X.; Yue, X.; Zhang, L.; Xu, X.; Liu, F.; Feng, M.; Hu, Z.; Yan, Y.; Scheuer, J.; Fu, X. Activated single photon emitters and enhanced deep-level emissions in hexagonal boron nitride strain crystal. *Adv. Funct. Mater.* **2024**, *34*, 2306128.

(31) Li, C.; Mendelson, N.; Ritika, R.; Chen, Y.; Xu, Z.-Q.; Toth, M.; Aharonovich, I. Scalable and deterministic fabrication of quantum emitter arrays from hexagonal boron nitride. *Nano Lett.* **2021**, *21*, 3626–3632.

(32) Sauvan, C.; Hugonin, J.-P.; Maksymov, I. S.; Lalanne, P. Theory of the spontaneous optical emission of nanosize photonic and plasmon resonators. *Phys. Rev. Lett.* **2013**, *110*, 237401.

(33) Goy, P.; Raimond, J.; Gross, M.; Haroche, S. Observation of cavity-enhanced single-atom spontaneous emission. *Phys. Rev. Lett.* **1983**, *50*, 1903.

(34) Anger, P.; Bharadwaj, P.; Novotny, L. Enhancement and quenching of single-molecule fluorescence. *Phys. Rev. Lett.* **2006**, *96*, 113002.

(35) Wang, Y.; Lee, J.; Berezovsky, J.; Feng, P. X.-L. Cavity quantum electrodynamics design with single photon emitters in hexagonal boron nitride. *Appl. Phys. Lett.* **2021**, *118*, 244003.

(36) Pors, A.; Bozhevolnyi, S. I. Quantum emitters near layered plasmonic nanostructures: decay rate contributions. *ACS Photonics* **2015**, *2*, 228–236.

(37) Vogl, T.; Lecamwasam, R.; Buchler, B. C.; Lu, Y.; Lam, P. K. Compact cavity-enhanced single-photon generation with hexagonal boron nitride. *ACS Photonics* **2019**, *6*, 1955–1962.

(38) Svendsen, M. K.; Ali, S.; Stenger, N.; Thygesen, K. S.; Iles-Smith, J. Signatures of non-Markovianity in cavity-QED with color centers in 2D materials. *Phys. Rev. Res.* **2023**, *5*, L032037.

(39) Häußler, S.; Bayer, G.; Waltrich, R.; Mendelson, N.; Li, C.; Hunger, D.; Aharonovich, I.; Kubanek, A. Tunable fiber-cavity enhanced photon emission from defect centers in hBN. *Adv. Opt. Mater.* **2021**, *9*, 2002218.

(40) Kim, S.; Fröch, J. E.; Christian, J.; Straw, M.; Bishop, J.; Totonjian, D.; Watanabe, K.; Taniguchi, T.; Toth, M.; Aharonovich, I. Photonic crystal cavities from hexagonal boron nitride. *Nat. Commun.* **2018**, *9*, 2623.

(41) Proscia, N. V.; Jayakumar, H.; Ge, X.; Lopez-Morales, G.; Shotan, Z.; Zhou, W.; Meriles, C. A.; Menon, V. M. Microcavity-coupled emitters in hexagonal boron nitride. *Nanophotonics* **2020**, *9*, 2937–2944.

(42) Parto, K.; Azzam, S. I.; Lewis, N.; Patel, S. D.; Umezawa, S.; Watanabe, K.; Taniguchi, T.; Moody, G. Cavity-enhanced 2D material quantum emitters deterministically integrated with silicon nitride microresonators. *Nano Lett.* **2022**, *22*, 9748–9756.

(43) Fröch, J. E.; Li, C.; Chen, Y.; Toth, M.; Kianinia, M.; Kim, S.; Aharonovich, I. Purcell enhancement of a cavity-coupled emitter in hexagonal boron nitride. *Small* **2022**, *18*, 2104805.

(44) Li, C.; Fröch, J. E.; Nonahal, M.; Tran, T. N.; Toth, M.; Kim, S.; Aharonovich, I. Integration of hBN quantum emitters in monolithically fabricated waveguides. *ACS Photonics* **2021**, *8*, 2966–2972.

(45) Spencer, L.; Horder, J.; Kim, S.; Toth, M.; Aharonovich, I. Monolithic integration of single quantum emitters in hBN bullseye cavities. *ACS Photonics* **2023**, *10*, 4417–4424.

(46) Tran, T. T.; Wang, D.; Xu, Z.-Q.; Yang, A.; Toth, M.; Odom, T. W.; Aharonovich, I. Deterministic coupling of quantum emitters in 2D materials to plasmonic nanocavity arrays. *Nano Lett.* **2017**, *17*, 2634–2639.

(47) Proscia, N. V.; Collison, R. J.; Meriles, C. A.; Menon, V. M. Coupling of deterministically activated quantum emitters in hexagonal boron nitride to plasmonic surface lattice resonances. *Nanophotonics* **2019**, *8*, 2057–2064.

(48) Xu, X.; Solanki, A. B.; Sychev, D.; Gao, X.; Peana, S.; Baburin, A. S.; Pagadala, K.; Martin, Z. O.; Chowdhury, S. N.; Chen, Y. P.; Taniguchi, T.; Watanabe, K.; Rodionov, A. I.; Kildishev, A. V.; Li, T.; Upadhyaya, P.; Boltasseva, A.; Shalaev, V. M. Greatly enhanced emission from spin defects in hexagonal boron nitride enabled by a low-loss plasmonic nanocavity. *Nano Lett.* **2023**, *23*, 25–33.

(49) Karanikolas, V.; Iwasaki, T.; Henzie, J.; Ikeda, N.; Yamauchi, Y.; Wakayama, Y.; Kuroda, T.; Watanabe, K.; Taniguchi, T. Plasmon-triggered ultrafast operation of color centers in hexagonal boron nitride layers. *ACS Omega* **2023**, *8*, 14641–14647.

(50) Kongsuwan, N.; Demetriadou, A.; Chikkaraddy, R.; Benz, F.; Turek, V. A.; Keyser, U. F.; Baumberg, J. J.; Hess, O. Suppressed quenching and strong-coupling of purcell-enhanced single-molecule emission in plasmonic nanocavities. *ACS Photonics* **2018**, *5*, 186–191.

(51) Mooradian, A. Photoluminescence of metals. *Phys. Rev. Lett.* **1969**, *22*, 185.

(52) Maksymov, I.; Besbes, M.; Hugonin, J.-P.; Yang, J.; Beveratos, A.; Sagnes, I.; Robert-Philip, I.; Lalanne, P. Metal-coated nanocylinder cavity for broadband nonclassical light emission. *Phys. Rev. Lett.* **2010**, *105*, 180502.

(53) Kühn, S.; Häkanson, U.; Rogobete, L.; Sandoghdar, V. Enhancement of single-molecule fluorescence using a gold nanoparticle as an optical nanoantenna. *Phys. Rev. Lett.* **2006**, *97*, 017402.

(54) Galloway, C.; Etchegoin, P.; Le Ru, E. Ultrafast nonradiative decay rates on metallic surfaces by comparing surface-enhanced Raman and fluorescence signals of single molecules. *Phys. Rev. Lett.* **2009**, *103*, 063003.

(55) Lassiter, J. B.; McGuire, F.; Mock, J. J.; Ciraci, C.; Hill, R. T.; Wiley, B. J.; Chilkoti, A.; Smith, D. R. Plasmonic waveguide modes of film-coupled metallic nanocubes. *Nano Lett.* **2013**, *13*, 5866–5872.

(56) Grossi, G.; Moon, H.; Lienhard, B.; Ali, S.; Efetov, D. K.; Furchi, M. M.; Jarillo-Herrero, P.; Ford, M. J.; Aharonovich, I.; Englund, D. Tunable and high-purity room temperature single-photon emission from atomic defects in hexagonal boron nitride. *Nat. Commun.* **2017**, *8*, 705.

(57) Senichev, A.; Martin, Z. O.; Peana, S.; Sychev, D.; Xu, X.; Lagutchev, A. S.; Boltasseva, A.; Shalaev, V. M. Room-temperature single-photon emitters in silicon nitride. *Sci. Adv.* **2021**, *7*, 0627.

(58) Orellana, W.; Chacham, H. Stability of native defects in hexagonal and cubic boron nitride. *Phys. Rev. B* **2001**, *63*, 125205.

(59) Gao, S.; Chen, H.; Bernardi, M. Radiative properties of quantum emitters in boron nitride from excited state calculations and Bayesian analysis. *Npj Comput. Mater.* **2021**, *7*, 85.

(60) Abdi, M.; Chou, J.; Gali, A.; Plenio, M. B. Color centers in hexagonal boron nitride monolayers: a group theory and ab initio analysis. *ACS Photonics* **2018**, *5*, 1967–1976.

(61) Mendelson, N.; Chugh, D.; Reimers, J. R.; Cheng, T. S.; Gottscholl, A.; Long, H.; Mellor, C. J.; Zettl, A.; Dyakonov, V.; Beton, P. H.; Novikov, S. V.; Jagadish, C.; Tan, H. H.; Ford, M. J.; Toth, M.; Bradac, C.; Aharonovich, I. Identifying carbon as the source of visible single-photon emission from hexagonal boron nitride. *Nat. Mater.* **2021**, *20*, 321–328.

(62) Neumann, M.; Wei, X.; Morales-Inostroza, L.; Song, S.; Lee, S.; Watanabe, K.; Taniguchi, T.; Götzinger, S.; Lee, Y. H. Organic molecules as origin of visible-range single photon emission from hexagonal boron nitride and mica. *ACS Nano* **2023**, *17*, 11679–11691.